Quantifying frost weathering induced damage in alpine rocks

Till Mayer[1,2], Maxim Deprez[3], Laurenz Schröer[3], Veerle Cnudde[3,4], Daniel Draebing[5,1]

[1] Chair of Geomorphology, University of Bayreuth, 95447 Bayreuth, Germany.
[2] Chair of Landslide Research, Technical University of Munich, 80333 Munich, Germany
[3] Department of Geology, University Gent, 9000 Gent, Belgium.
[4] Department of Earth Sciences, Utrecht University, 3584 CB Utrecht, Netherlands.
[5] Department of Physical Geography, Utrecht University, 3584 CB Utrecht, Netherlands.

Correspondence to: Till Mayer (till.mayer@uni-bayreuth.de)

Abstract. Frost weathering is a key mechanism of rock failure in periglacial environments and landscape evolution. At high alpine rockwalls, freezing regimes are a combination of diurnal and sustained seasonal freeze-thaw regimes and both influence frost cracking processes. Recent studies have tested the effectiveness of freeze-thaw cycles by measuring weathering proxies for frost damage in low-strength and grain-supported pore space rocks, but detecting frost damage in low-porosity and crack-dominated alpine rocks is challenging due to small changes in these proxies that are close to the detection limit. Consequently, the assessment of frost weathering efficacy in alpine rocks may be flawed. In order to fully determine the effectiveness of both freezing regimes, freeze-thaw cycles and sustained freezing were simulated on low-porosity high-strength Dachstein limestone with varying saturation. Frost-induced rock damage was uniquely quantified by combining X-ray computed micro-tomography (μCT), acoustic emission (AE) monitoring and frost cracking modelling. To differentiate between potential mechanisms of rock damage, thermal- and ice-induced stresses were simulated and compared with AE activity. Our results underscore the significant impact of initial crack density on frost damage, with μCT scans revealing damage primarily through crack expansion. Discrepancies between AE signals and visible damage indicate the complexity of damage mechanisms. The study highlights frost cracking as the main driver of rock damage during freezing periods. Notably, damage is more severe during repeated freeze-thaw cycles compared to extended periods of freezing, a finding that diverges from field studies. This discrepancy could stem from limited water mobility due to low porosity or the short duration of our experimental setup.

Keywords. Frost weathering, μCT, periglacial processes, frost cracking modelling, rock damage

1 Introduction

Frost weathering is a key mechanism for rock breakdown in periglacial environments (Matsuoka and Murton, 2008) and is therefore considered to be the main driver for alpine landscape evolution (Egholm et al., 2015; Hales and Roering, 2009). The

breakdown of rock due to freezing is called frost cracking and can prepare and trigger rockfall (Matsuoka, 2019). Cracking can occur when stresses exceed thresholds (critical cracking) or by repetition of low magnitude stresses that progressively weaken the rock (subcritical cracking; Eppes and Keanini, 2017). Frost cracking was associated with two different processes:
35 volumetric expansion and ice segregation (Matsuoka and Murton, 2008).

When water freezes to ice volumetric expansion of 9% occurs and can theoretically build up stresses of up to 207 MPa (Matsuoka and Murton, 2008), which would exceed the tensile stress of most existing rock (Perras and Diederichs, 2014). Conditions that favour volumetric expansion are a high degree of water saturation of 91 % (Walder and Hallet, 1986), a rapid freezing associated with diurnal freeze-thaw cycles (Matsuoka, 2001; Matsuoka and Murton, 2008) and a freezing from all
40 sides (Matsuoka and Murton, 2008). However, conditions facilitating volumetric expansion in real rockwalls are rare as moisture conditions exceeding 91 % are rarely given during phases of rapid freezing (Sass, 2005a).

During freezing processes, ice crystals develop within cracks and pores of rock. A repulsion mechanism ensures that a thin water film (<9 nm) persists between the ice crystal and the walls of the pore or crack (Gilpin, 1979; Webber et al., 2007; Sibley et al., 2021), facilitating the movement of unfrozen water present within the frozen rock matrix towards the ice crystal driven
45 by a thermodynamic potential gradient (Derjaguin and Churaev, 1986; Kjelstrup et al., 2021; Everett, 1961; Gerber et al., 2022). Due to ice segregation, ice expands within pores and cracks and generates crystallization pressure (Scherer, 1999) that can damage rocks. Ice segregation is most efficient in a temperature range called the 'frost cracking window' (Anderson, 1998) which depends on rock strength (Walder and Hallet, 1985; Mayer et al., 2023). Common temperature ranges vary from -6 to -3 °C for low-strength Berea sandstone (Hallet et al., 1991), but can drop to -15 to -5°C for high-strength rocks (Walder and
50 Hallet, 1985; Mayer et al., 2023). Ice segregation can occur in low-saturated rock (Mayer et al., 2023) and is theoretically more conducive in environments characterized by slow freezing rates and continuous low temperatures typical of seasonal freezing (Matsuoka and Murton, 2008; Walder and Hallet, 1986).

Frost cracking serves as an indicator for assessing frost damage or the increase in porosity in rocks and rockwalls, yet its gradual and subcritical nature makes direct measurements challenging. Consequently, laboratory studies have adopted
55 indicators such as AE signals (Hallet et al., 1991; Mayer et al., 2023; Maji and Murton, 2021; Duca et al., 2014), frost heave or crack expansion (Murton et al., 2006; Draebing and Krautblatter, 2019), alterations in mechanical properties like p-wave velocity, Youngs' Modulus, uniaxial strength or porosity (Whalley et al., 2004; Matsuoka, 1990; Jia et al., 2015; Eslami et al., 2018; Prick, 1997), and frost cracking simulations (Mayer et al., 2023; Murton et al., 2006) to estimate its impact. At the scale of rockwalls, proxies such as AE signals (Girard et al., 2013; Amitrano et al., 2012), fracture density (Hales and Roering, 2009;
60 Draebing and Mayer, 2021; Messenzehl et al., 2018), fracture opening (Draebing, 2021; Draebing et al., 2017b; Draebing et al., 2017a), rockwall erosion rates (Draebing et al., 2022; Matsuoka, 2008), as well as frost cracking simulations (e.g. Draebing et al., 2022; Sanders et al., 2012) have been utilized to infer frost cracking activity. However, all these techniques provide proxies for frost cracking and as low-porosity alpine rocks are characterized by micro-cracks, changes in frost cracking proxies are very small and often within the uncertainty of the techniques used, and therefore do not provide reliable results. In contrast,
65 X-ray computed micro-tomography (μCT) enables the quantification of material damage (Cnudde and Boone, 2013; Withers

et al., 2021) and was previously applied to track frost cracking damage in high-porosity rocks (De Kock et al., 2015; Deprez et al., 2020a; Maji and Murton, 2020; Dewanckele et al., 2013) or assess post-experimental frost damage along artificial cracks in low- porosity rocks (Wang et al., 2020a; 2020b) exposed to frequent freeze-thaw cycles.

To our knowledge, no study has directly quantified the effectiveness of different freeze-thaw cycles or demonstrated whether frost cracking creates new cracks or propagates existing cracks in high-strength, low porosity rocks. In this study, we exposed low-porosity, high-strength Dachstein limestone to frequent diurnal and seasonal sustained freeze-thaw cycles during laboratory freezing experiments. We monitor acoustic emission events during the experiments and modelled thermal and ice-induced stresses and applied μCT to pre- and post-stressed rocks to quantify and track crack propagation and to assess frost cracking efficacy of different freeze-thaw cycles.

2 Material and Methods

2.1 Rock samples and mechanical properties

We collected three large boulders of Dachstein limestone in the Dachstein mountain range, Austria. Dachstein limestone (upper Triassic) is a massive rock with minor occurrence of fractures which is widespread in the Northern-Calcareous Alps (Pfiffner, 2010). From boulder one, we drilled three cylindrical samples with 10 cm (in length) x 5 cm (in diameter) and measured rock density ρ_r and open porosity n_r by immersion weighing (DIN-EN 52102:2006-02; DIN-EN 1097-6:2022-5). The determined rock density was 2690 kg m^{-3} and rock porosity 0.1% (Table 1). To quantify shear modulus G, Poisson' ratio v and Young's modulus E, dilatational wave velocity measurements were performed using a Geotron ultrasonic generator USG40 and a Geotron preamplifier VV51 with 20 kHz sensors. Sensor to sample coupling was improved by applying 0.2 MPa pressure. Detection and analyses of the signals were proceeded with a PICO oscilloscope and the software Geotron Lighthouse DW. Determined values of shear modulus were 24.02 ±0.05 GPa, Poisson' ratio 0.327 ±0.003 and Young's modulus 63.74 ±0.04 GPa (Table 1). We drilled two cylindrical samples with a size of 5 x 2.5 cm from boulder one to measure tensile strength σ_t following Lepique (2008). The determined tensile strength was 7.9±0.7 MPa. Fracture toughness K_{iC} was tested in the Magnel-Vandepitte Laboratory at Ghent University using a three-point bending test setup on boulder two (Carloni et al., 2019; Bazant and Planas, 1998). For Dachstein limestone the fracture toughness was 1.32±0.1 MPa m$^{1/2}$. For the freezing experiments we drilled six cylindrical samples 91.5 mm long and 25.5 mm in diameter from boulder three (Fig. 1b) to keep micro-fractures as homogenous as possible. We assume that mechanical properties from the three rock boulders are identical as they were collected from the same rockwall.
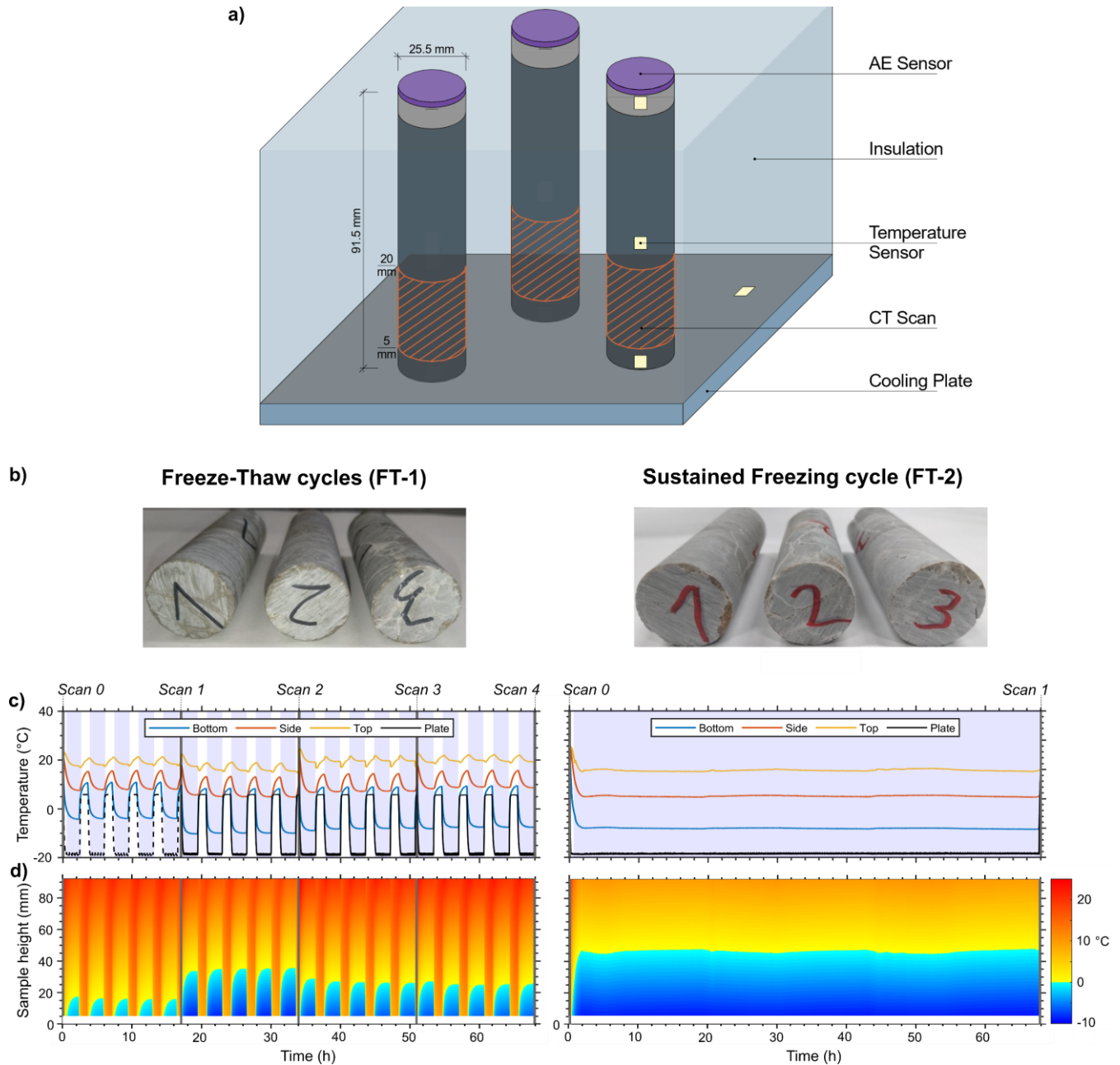
Figure 1: The design of the experiment was influenced by the methodologies of Hallet et al. (1991) and Mayer et al. (2023), focusing on distinguishing ice segregation as a distinct weathering process from other weathering mechanisms. a) Schematic representation of freezing laboratory setup. We created a linear temperature gradient by cooling three rock samples, each with varying levels of saturation, using a cooling plate positioned at the bottom, while exposing the top of the samples to ambient room temperature conditions. b) 91.5 x 25.5 mm large cylindrical Dachstein limestone samples used for freeze-thaw experiments. c) temperature cycles were implemented for FT-1 and FT-2, along with the corresponding measurements of rock and cooling plate temperatures. In FT-1, between scan 0 and 1, there was inadequate coupling of the temperature sensor, resulting in excessively high temperature readings. d) temperature isoplots of derived temperature distribution within the sample.

2.2 Freezing experiments setup

Three rock samples were placed at the same time into an insulating holder on a cooling plate, which was driven by Peltier elements (TE technology, CP-121HT), a power supply unit (PS-24-13), and a temperature control system (TC-48-20 OEM, Fig. 1a). While the bottom part was exposed to freezing conditions from the cooling plate, the top part was left open to non-freezing ambient laboratory conditions (~20 °C). With this setup we simulated a closed system that provides a linear temperature gradient and a water body inside the rock samples reflecting simplified natural rockwall conditions. During the freezing experiments, rock temperature was monitored every minute at the side close to the top, middle and close to the bottom of one rock sample with three SE060 high temperature type K thermocouples (accuracy ±0.5 °C, Pico Technology, Fig. 1b) to avoid damaging the samples by drilling. The surface temperature of the sample has a slight offset compared to the internal temperature at the centre, with lower temperatures in the core of the sample. However, we assume this offset as minor due to the high thermal conductivity of limestone (2.4 Wm-1K-1 (Cermák and Rybach, 1982). An additional thermocouple was placed onto the cooling plate to record cooling plate temperatures. To test the efficiency of freeze thaw cycles, we exposed three rock samples at the same time to two different freeze-thaw cycles.

As saturation influences frost weathering, we used rock samples with an initial saturation of approximately 30, 70 and 100 % categorized as low, partially, and highly saturated, respectively. The samples were saturated by immersing the lower part into a distilled water bath. To prevent air inclusions, we raised slowly the water table until samples were completely immersed, and a constant mass was prevailing (we refer to as highly saturated). Subsequently, samples were dried under atmospheric conditions, weighed until low (30 %) or partially saturation (70 %) was reached. To minimize moisture loss through evaporation, the samples were wrapped in clingfilm. As porosity of the samples is 0.1 %, the level of saturation is inaccurate and provide only a rough estimation. Furthermore, the saturation can change during the experiments due to moisture loss or distribution of rock moisture can alter within the rock samples. We chose the length of the rock samples of 91.5 mm to enable moisture migration towards the sample parts close to the cooling plate where freezing occurred. Due to the low number of samples, we cannot quantify saturation effects on frost weathering, however, our set up enables us to incorporate the variability of saturation levels occurring in natural rockwalls and to test the consistency of frost damage patterns.

To monitor acoustic emission (AE) which are used as a proxy for cracking (Eppes et al., 2016; Hallet et al., 1991), a Physical Acoustics AE sensor PK6I with a frequency between 35 and 65 kHz was mounted with acrylic sealant on top of each rock sample (Fig. 1a). The detected AE signals were recorded with a Physical Acoustics micro SHM node. Recorded data were subsequently processed and filtered using Physical Acoustics AEwin software. Due to low background noises of our setup, we set an initial signal threshold of 30 dB$_{AE}$, which is similar to Mayer et al. (2023) who established a threshold of 35 dB$_{AE}$, due to the presence of stronger background noises. We performed lead break tests as sample cracks (Eppes et al., 2016) before and after each scan to control sensor coupling and evaluating system performance and wavelength form. Poor coupling of an AE sensor could lead to diminished AE amplitudes, meaning signals of low amplitude might not be detected by the system. To

avoid erroneous AE signals stemming from the setup, the system underwent testing without any freezing or temperature alterations.

During freezing test 1 (FT-1), we simulated diurnal freeze-thaw conditions and exposed three samples with different saturation levels (Fig. 1b) to 20 freeze-thaw cycles (Fig. 1c). In each cycle, we cooled down the samples until the cooling plate reached -20 °C and the rock temperature at the bottom of the samples was approximately -10 °C followed by one hour warming until a cooling plate temperature of 5 °C and sample temperatures between 5 and 7°C were achieved. Small sample temperature deviations could occur due to thermistor placement at the side of the sample or ice development between cooling plate and rock samples. Our set up enabled us to develop a thermal gradient within the samples (Fig. 1d) where the lower part of the rock samples between 0 and 40 mm sample height including the scanned area between 5 mm and 19 mm sample height (Fig. 2a) were exposed to freezing conditions while the upper parts remain unfrozen. The freezing rate we utilized, 12.5°C per hour at the cooling plate, might surpass those observed in natural rockwall settings, yet it is comparable to the rates employed in earlier freezing studies (Jia et al., 2015; Matsuoka, 1990). The applied freezing rate could amplify frost cracking and result in an overestimation of frost damage.

In our second experiment, we subjected three rock samples, each with varying levels of saturation (Fig. 1b), to an extended period of freezing (FT-2), maintaining the cooling plate at -20 °C for 68 hours. This setup resulted in a temperature gradient within the samples, with the lower 0-40 mm of the samples experiencing freezing temperatures and the upper section remaining above freezing, maintaining a stable thermal gradient for about 66 hours (Fig. 1d). The setup aimed to enable the migration of water from the unfrozen segment to the frozen one enhancing the potential for frost cracking; however, the sample's low porosity combined with the small size of the unfrozen segment limits the amount of water that can migrate, potentially resulting in an underestimation of frost damage compared to what might be observed in natural conditions.

2.3 μCT imaging

In order to identify crack locations and quantify crack growth, X-ray computed micro-tomography (μCT) was performed at the Ghent University Centre for Tomography (UGCT) with the CoreTom (TESCAN XRE) μCT scanner. For experiment FT-1, μCT scans were performed before the start and after every five cycles (Fig. 3). For the sustained freezing experiment (FT-2), rock samples were scanned before and after the experiment. As only the bottom part of the sample (0 – 40 mm) experiences freezing (Fig. 1c-d), the rock sample sections between 0 and 20 mm were scanned (Fig. 2a). The dimension of the section was determined to optimize the resolution, as the resolution of scanning is influenced by the size of the sample (Cnudde and Boone, 2013). The μCT system settings for our experiment were set to 179 kV for the X-ray source with a power output of 20 W. The scans were performed at binning 2 and a voxel size of 20 μm. A one mm thick aluminium plate was used to filter low energy X-rays and reduce beam hardening. For each sample 2142 projections were made with an exposure time of 600 ms. The raw μCT data was reconstructed using the software PANTHERA (TESCAN XRE) where beam hardening and ring filters were applied, and which resulted in a stack of cross-sections saved as 16-bit tiff. Images. All subsequent image handling, such as registration, segmentation, and analyses, were performed with Avizo3D Pro (Version 2021.1, ThermoFisher Scientific). In

Avizo, a sandbox filter was conducted to bin contrast variations inside the images and match contrast between the single scans. We tuned the parameters until visually the best result was observed. Therefore, sample voids (pore space) and matrix (sample material) of each image could be separated by thresholding over contrast. We followed the work after Deprez et al. (2020a) and defined a distinguishable feature in the scan image as a minimum spatial resolution of 3 times the voxel size (60 µm). Volume fractions and the expansion of pore space in the sample were assessed using photogrammetry in Avizo. For each image, the software detected and quantified distinctions between void voxel V_V and the matrix voxel V_M which we call crack fraction cf (Fig. 2b). Crack fraction is derived by:

$$cf = \frac{V_V}{V_V + V_M} \tag{1}$$

 This approach enabled subsequent comparisons between scans to assess the development of pore space growth in the sample (Fig. 2c,d). The parameter crack fraction was defined by the total amount of segmented pore space (voids) per image in the image stack (cross section) divided by the total amount of segmented sample material (matrix + voids). Due to effects of beam hardening, which result in image distortion at sample heights between 0 and 5 mm and between 19 and 20 mm, our analyses were concentrated on the portion of the rock sample ranging from 5 to 19 mm in height. We quantified crack growth (pore space growth) by comparing the crack fraction per layer after each scan (Fig. 2d and 6a-f).

If growth occurs in every crack or void, this implies that the distribution of initial cracks/voids could either accelerate or decelerate the growth of cracks. Consequently, crack growth cannot be directly compared across samples due to variations in crack distribution. To address this, we adjusted each scan cf_i by its initial crack fraction cf_0, allowing for an assessment of crack growth that is independent of the initial crack distribution. The normalized crack fraction, cf_{norm} for each scan is calculated as follows:

$$cf_{norm,i} = \frac{cf_i}{cf_0}, \tag{2}$$

where i represents the scan number. For the purpose of assessing the progression of quantified frost damage both within a single sample and among different samples, we computed the mean of cf_{norm} for each scan.
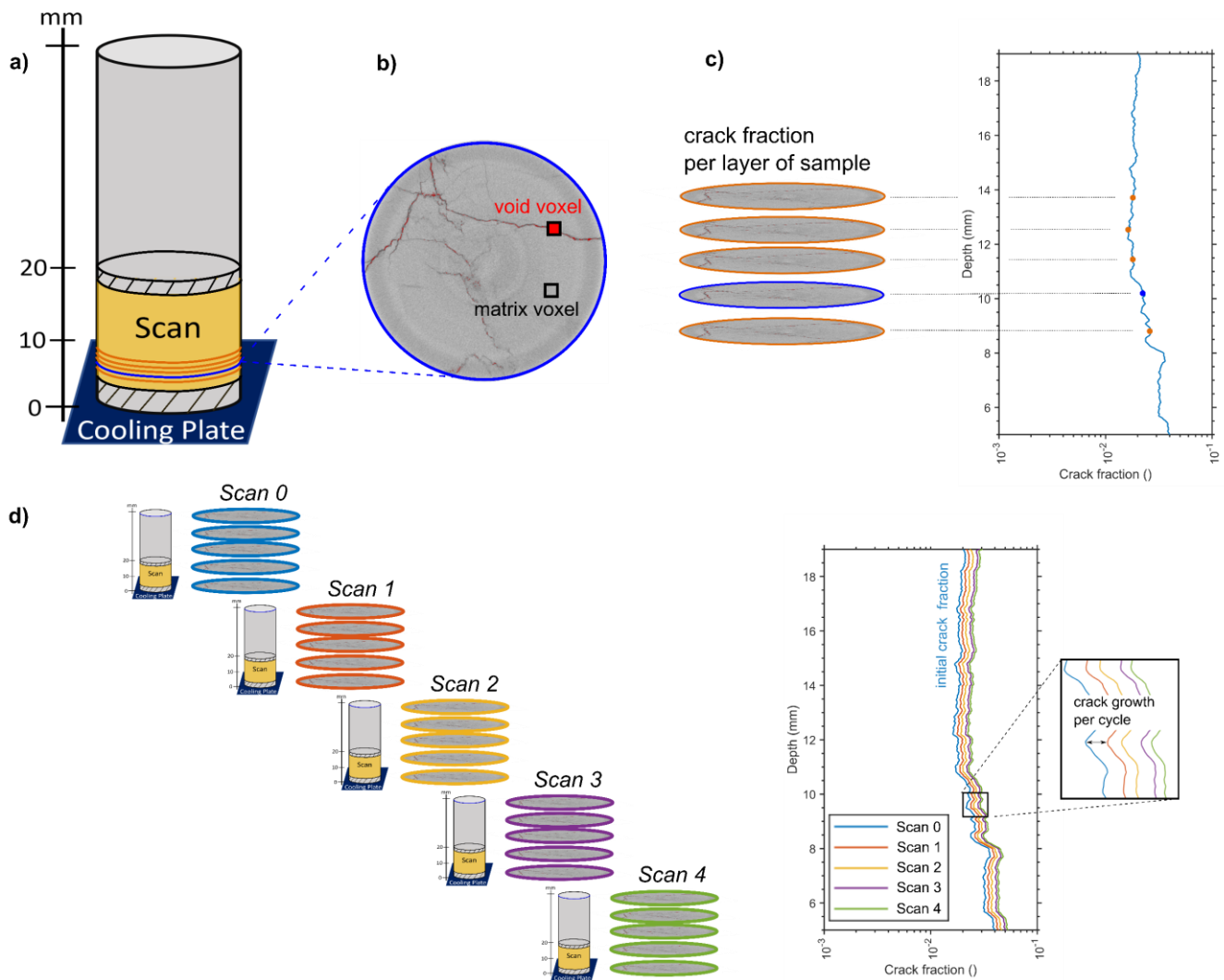
Figure 2: Schematic drawing from scan to crack growth. a) scanned volume from 0 – 20 mm sample height. Due to beam hardening effects (black dashed area) at the edges only the area between 5 - 19 mm sample height was analysed. b) Example scan of one layer (20 µm thick) with example void/crack voxel and matrix voxel derived by Avizio3D Pro. c) Crack fraction derived for each layer over the whole scanned height from 5 - 19 mm by photogrammetry. d) Example of resulting crack growth per cycle with initial crack fraction (blue line).

2.4 Thermal- and ice-stress modelling

We modelled thermal and ice stresses to determine potential drivers of AE signals and porosity growth. The models require a one-dimensional temperature distribution inside the samples. Temperature distributions were calculated by assuming a linear and homogeneous temperature gradient between all temperature sensors (Fig. 1d,e). Latent heat effects were incorporated in general as our sensors measured rock temperatures which were affected by latent heat effects. All thermal and ice stress

8

simulations were performed in MATLAB (2021). Thermal stress occurred in our samples as a result of changing temperatures. We modelled one-dimensional thermal stress σ_{TL} after Paul (1991):

205
$$\sigma_{TL}(t) = 2 \cdot G \cdot \alpha_T \left| \frac{dT_{L\pm5}}{dt} \right| (1 + v), \tag{3}$$

with thermal expansion coefficient α_T, shear modulus G and Poisson ratio v (Table 1). $T_{L\pm5}$ represents a running temperature mean over five minutes. Our model approach did not incorporate complex crack geometries of the samples; therefore, we could only provide quantitative estimates of thermal stress. Hence, we focused in our analysis on timing of thermal stresses and did not analyse absolute stress values.

210

We applied frost cracking modelling to determine when ice stresses occur during the tests. Frost cracking modelling was performed using the model of Walder and Hallet (1985), which combines hydraulic and mechanic rock properties. The model simulated ice pressures in a single 1 mm long mode I crack. Therefore, this model simplified crack geometry and provided quantitative estimates of ice pressures. Due to the abstract model predictions, we used quantified ice pressures only to interpret

215 the timing of AE events and not to relate ice pressure to rock damage. We will test different parameter influences on model prediction in a sensitivity analyses (see Fig. S1 and S2 in Supplementary Information). The basic model requirement to start ice segregation are rock temperatures below the pore freezing point T_f and an unfrozen area inside the rock, which acts as a water reservoir (Fig. 1d). The transition area between a potential ice lens in the frozen part and the unfrozen area is called frozen fringe. The model assumes a fully saturated rock. Ice pressure rises between lens and pore/crack wall when water

220 migration is driven by a thermodynamic potential gradient through the frozen fringe. The amount of supplied water is governed by Darcy's law but restrained due to hydraulic conductivity inside the frozen fringe and flow resistance due to the thin film between ice and crack wall.

Following Walder and Hallet (1985), we chose a hydraulic conductivity of k_{hc} of 5×10^{-14} m s^{-1}. Flow resistance between the

225 ice and pore wall depends on grain size R, liquid-layer thickness h_l, and ice-free porosity n_f. Walder and Hallet (1985) set the grain size to 0.75 mm, the liquid-layer thickness to 6 nm °C$^{1/2}$ (after Gilpin (1980) at a temperature of -1 °C) and neglected ice-free porosity. A simplified potential ice lens has the form of a penny-shaped crack with a crack radius c and a width w. With water migrating towards the ice lens, ice pressure rises inside the lens and finally leads to tip cracking (mode I type). The initial crack length (two times the crack radius) is set between 1 and 40 mm with crack orientation parallel to the sample bottom

230 (φ_p=0 °). After Walder and Hallet (1985) shear modulus G and Poisson' ratio v determine how the penny-shaped crack is deformed elastically into an oblate ellipsoid when ice pressure p_i is applied and be described for very thin cracks (w<<c) to

$$\frac{w(n,t)}{c(n,t)} = \frac{4}{\pi} \left(\frac{1-v}{G} \right) p_i. \tag{4}$$

where n represents the incremental depth (1 mm), and t denotes the incremental timing (1 min). The crack finally breaks subcritical inelastically at the tip (mode I type) and propagates at a growth rate V when one third of the critical fracture

235 toughness K_C ($K_* = 1/3K_c$) is exceeded, for $K_I > K_*$ crack growth can be expressed after Walder and Hallet (1985) as:

$$V = V_c[e^{\gamma(\frac{K_I^2}{K_c^2}-1)} - e^{\gamma(\frac{K_*^2}{K_c^2}-1)}],$$ (5)

with K_I being the stress intensity factor and $V=0$ when $K_I \leq K_*$. Subcritical cracking can be also expressed by the critical ice pressure (13.7 MPa) which is derived from transforming $K_I=(4c/\pi)^{1/2}p_i$ from Walder and Hallet (1985) and incorporating the measured critical fracture toughness of 1.32±0.1 MPa m$^{1/2}$ and an initial crack length of 1 mm. We set the dependent growth law parameters V_c and γ to be 340 m s^{-1} and 37.1 (Table 1) after Westerly granite (Walder and Hallet, 1985). Our model simplifies the complex process of frost weathering in natural rock. We conducted a sensitivity analysis to assess the impact of various rock parameters and selected the optimal value based on these findings (see Supplementary S1-2 and section 4.4).

Table 1. Parameters used for thermal stress and frost cracking modelling of Dachstein Limestone samples.

Parameter		Value
Ice density (kg m^{-3})	ρ_i	920
Water density (kg m^{-3})	ρ_w	1000
Pore freezing point (°C)*	T_f	-1
Hydraulic conductivity (m s^{-1})*	k_{hc}	5x10^{-14}
Grain size (mm)*	R	0.75
Liquid layer thickness (nm °C$^{1/2}$)*	h_l	6
Initial crack length (mm)*	x_i	1,20,40
Angle between crack plane and rock wall (°)*	ϕ	0
Poisson' ratio ()	ν	0.327 ±0.033
Critical fracture toughness (MPa m$^{1/2}$)	K_C	1.32 ±0.13
Growth-law parameter (m s^{-1})*	V_c	340 ±34
Growth-law parameter ()*	γ	37.1 ±3.7
Rock density (kg m^{-3})	ρ_r	2690
Rock porosity (%)	n_r	0.1
Shear modulus (GPa)	G	24.02±2.4
Young's modulus (GPa)	E	63.74
Thermal expansion coefficient (°C^{-1})+	α_T	6 x 10^{-6}

* Walder and Hallet (1985), + Pei et al. (2016)

3 Results

3.1 Continuous AE and temperature monitoring and stress modelling

#### 3.1.1 Freeze-Thaw cycles (FT-1)

The rock samples' bottom was exposed to a temperature range of -19 to 6 °C by the cooling plate. Initial temperature loggers were poorly attached to the rock, causing discrepancies in bottom surface temperatures during the first five freeze-thaw cycles compared to later cycles, as shown in Fig. 3a, suggesting that the actual temperatures were likely lower than those recorded.

After five cycles, a temperature sensor was added to the cooling plate. Between freeze-thaw cycles 5 and 20 the bottom rock temperature reached minimal temperatures of -10 to -8 °C and maxima of 8.5 to 9.5 °C, while the top sensor consistently registered 15 to 24 °C.

More AE hits were recorded during freezing phases compared to non-freezing ones (Fig. 3c). The majority of hits occurred when bottom temperatures were below freezing, with the highly saturated sample registering 235 hits, the partly saturated sample 326 hits, and the low saturated sample 123 hits. Positive temperature readings yielded fewer hits: 82 for the highly saturated, 89 for the partly saturated, and 57 for the low saturated samples. Total AE hits observed were 317 for the highly saturated sample, 415 for the partly saturated sample, and 180 for the low saturated sample.

Throughout the cycles, a pattern of accumulating AE hits among the samples is evident. Initially, the highly saturated sample accumulated the majority of hits in the first 10 cycles (121 hits). However, there was a notable increase in AE hits for the partly saturated sample, eventually leading to a higher total than the highly saturated sample between 10 and 20 cycles (173 hits). Given the consistent trend observed in both the highly and low saturated samples, a likely shift in the coupling between the AE sensor and the sample is suggested. Consequently, it is probable that the total AE hits for the partly saturated sample were fewer than those for the highly saturated one. Due to two recording interruptions of the AE logger, AE hits for the FT-1 cycle are likely underestimated.
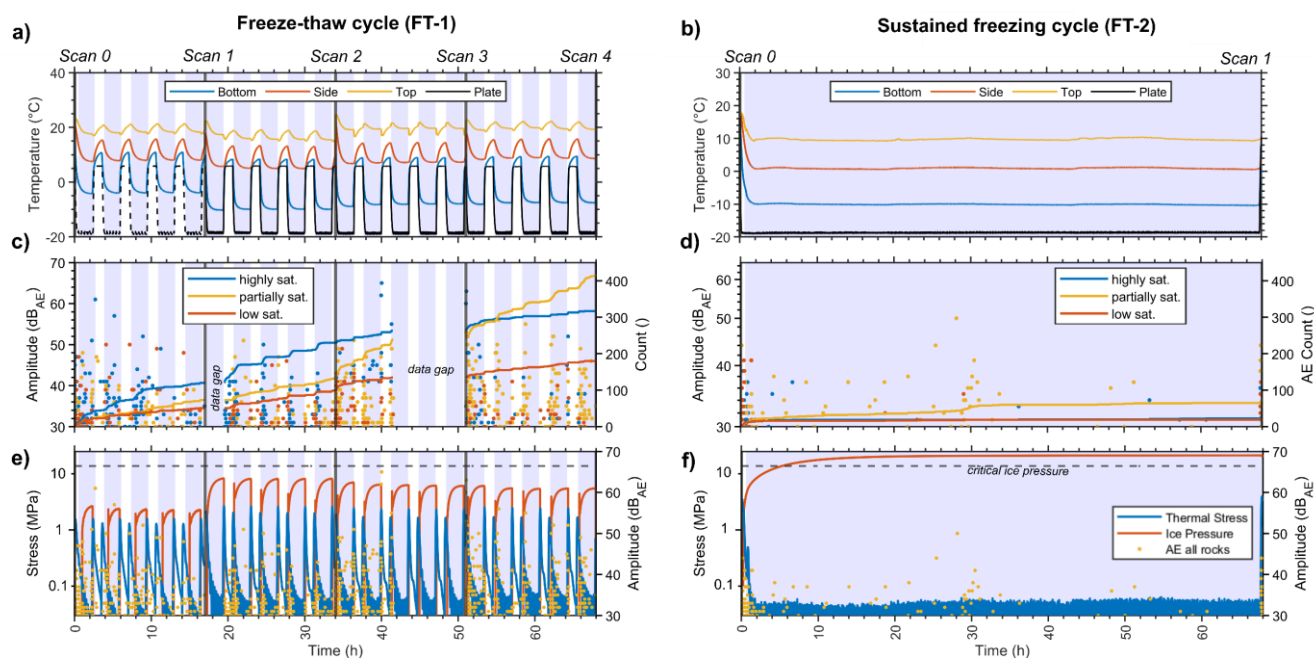
Figure 3: FT-1 resulted in significantly more AE hits than FT-2, as indicated by thermal stress models but not reflected in frost cracking models where FT-2 showed higher predicted ice stresses. More AE hits were recorded during freezing phases compared to non-freezing ones. a-b) Respectively measured rock and cooling plate temperatures, c-d) recorded AE hits (coloured dots) and cumulative AE hits (coloured lines), and e-f) modelled thermal and ice stresses at bottom temperature sensor plotted against time for FT-1 and FT-2 with AE hits from all samples. The dashed black line highlights cooling plate temperatures according to the

11

controller while black lines indicated measured plate temperature (cooling plate sensor was attached after first 5 cycles). The temperature offset between scan 0 and 1 during FT-1 (a) is a result of poor connectivity of the bottom temperature sensor. Blue backgrounds highlight periods when bottom rock samples were exposed to temperatures below 0 °C.

280 Our model indicated that both thermal- and ice-induced stresses peaked during freezing temperatures (Fig. 3e). However, due to a temperature discrepancy in the initial five freeze-thaw cycles, the modelled thermal and ice stress were underestimated (Fig. 3e). From the fifth to the twentieth cycle, the highest thermal stresses occurred as temperatures transitioned from thawing to freezing, reaching pressures of 2.15 ± 0.25 MPa and 2.95 ± 0.20 MPa respectively. These stresses were minimal at stable temperatures. Ice stress was present only during freezing, with the model predicting increasing ice stresses up to a maximum

285 of 6.85 ± 1.35 MPa at the end of each freezing phase. This is significantly below the critical ice pressure threshold (13.7 MPa) for subcritical cracking.

3.1.2 Sustained freezing cycle (FT-2)

In the FT-2 run, the partially saturated sample registered the highest number of AE hits, with ice stresses being a major factor.

290 The rock samples underwent 68 hours of freezing, maintaining a constant bottom temperature of -10 ± 0.5 °C (Fig. 3b). During this period, the middle sensor recorded a slightly positive temperature of 0.9 ± 0.3 °C, and the top sensor stayed at 9.8 ± 0.4 °C. AE logging revealed 28 hits for the highly saturated, 77 hits for the partially saturated, and 23 hits for the low saturated sample (Fig. 3d). The fixed freezing phase caused 11 hits to occur at the highly saturated rock, 53 hits at the partly saturated rock and 8 hits at the low saturated rock. Thermal stress modelling indicated peak stresses of 3.6 MPa during cooling and 3.9 MPa

295 during warming at the cycle's start and end (Fig. 3f), dropping below 0.1 MPa at stable temperatures. Ice stress models showed a continuous increase in ice stress throughout the freezing phase, reaching a maximum of 21 MPa, surpassing the critical ice pressure threshold of 13.7 MPa after 5.4 hours.

300 ## 3.2 Discontinuous µCT monitoring

3.2.1 Freeze-Thaw cycles (FT-1)

Conducted with a spatial resolution of 60 µm, the µCT scans indicated that the majority of the pore volume in our samples consisted of cracks, with changes in volume manifesting as crack expansion (Fig. 4). The expansion of cracks was found to be consistent throughout the height of the sample, indicating that the growth of cracks was uniform from the topmost scanned

305 section (19 mm) to the lowest (5 mm), However, there was a discernible positive relationship between initial crack and subsequent crack growth (Fig. 5a-c). Crack fraction in the initial scan (scan 0) before freezing exhibited variations from $0.023^{+0.019}_{-0.009}$ in the low saturated rock, $0.006^{+0.005}_{-0.002}$ in the partially saturated rock, and $0.007^{+0.005}_{-0.002}$ in the highly saturated rock.

The final (scan 4) crack fraction was $0.031^{+0.028}_{-0.009}$ (an increase of 35 %) for the low saturated rock, $0.008^{+0.006}_{-0.004}$ (an increase of 33 %) for the partially saturated rock, $0.011^{+0.006}_{-0.003}$ (an increase of 51 %) for the highly saturated sample.
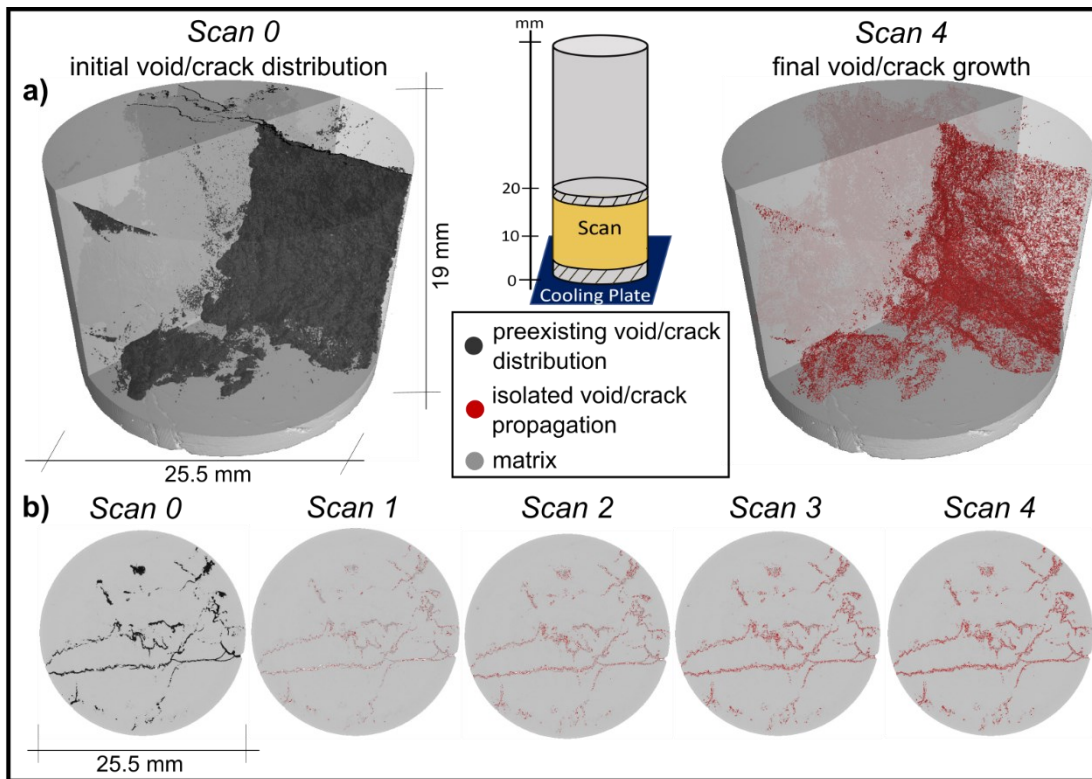
310

To mitigate the influence of initial crack distribution on crack growth analysis, we normalized the growth of crack volume for each sample relative to its initial crack fraction (see Eq. 2). This normalization showed that crack growth was consistent throughout the sample's height, though the extent of growth varied with saturation levels (Fig. 5g-i). Scan 4 revealed a final mean normalized crack growth of 1.34 ±0.8 (equivalent to 34% more crack volume than the initial value) for the low saturated sample, 1.29 ±0.11 (29% increase) for the partially saturated sample, and 1.52 ±0.13 (52% increase) for the highly saturated sample. The mean normalized increase in crack volume between scans was 0.8 ±0.03 (8% increase) for the low saturated sample, 0.07 ±0.04 (7% increase) for the partially saturated sample, and 0.13 ±0.05 (13% increase) for the highly saturated sample.
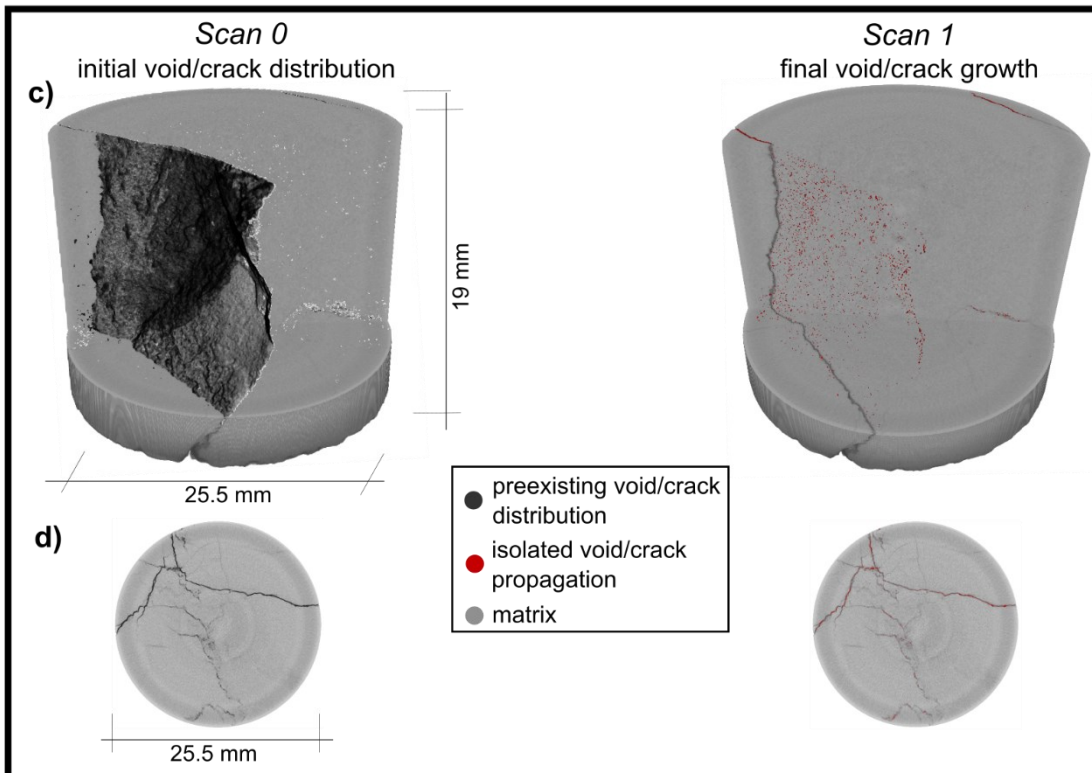
320

Freeze-thaw cycle (FT-1)

a)
Scan 0
initial void/crack distribution

Scan 4
final void/crack growth

19 mm

25.5 mm

mm
Scan
Cooling Plate
20
10
0

● preexisting void/crack distribution
● isolated void/crack propagation
● matrix

b)
Scan 0   *Scan 1*   *Scan 2*   *Scan 3*   *Scan 4*

25.5 mm

Sustained freezing cycle (FT-2)

c)
Scan 0
initial void/crack distribution

Scan 1
final void/crack growth

19 mm

25.5 mm

● preexisting void/crack distribution
● isolated void/crack propagation
● matrix

d)

25.5 mm

Figure 4: μCT visualizes crack growth at both cycles FT-1 and -2. a) 3D μCT scans before (scan 0) and after the last freeze-thaw cycle (scan 4) of low-saturated rock sample experiencing FT-1 and c) partially saturated rock sample. The initial distribution of cracks/voids is depicted in black, whereas red illustrates solely the isolated growth of these cracks. Example of μCT scan slices at 8 mm height from the bottom for b) the low saturated sample exposed to FT-1 and d) for the partially saturated samples experiencing FT-2.
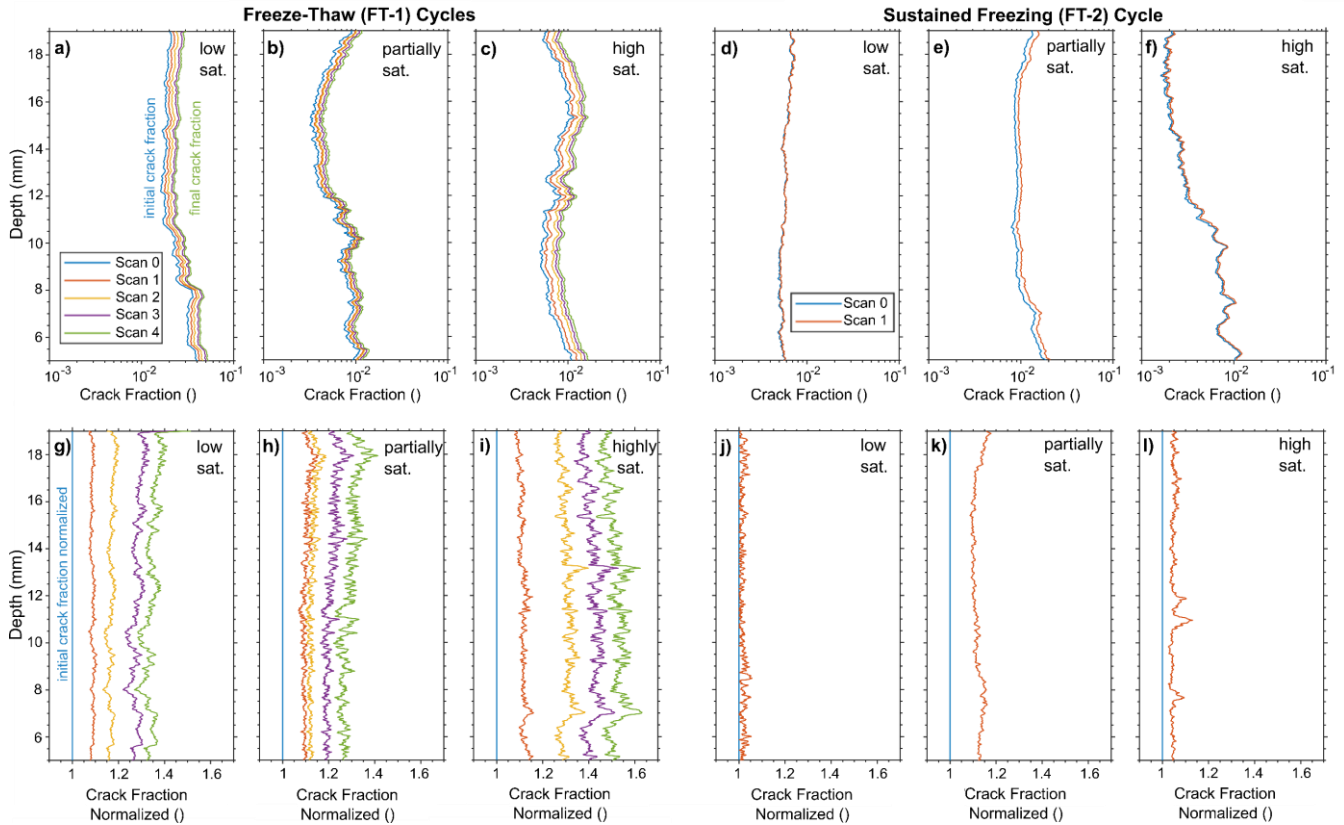
Figure 5: μCT effectively showcases the progression of cracks in our samples, illustrating a steady growth in crack volume that is uniform throughout different heights in the sample and directly correlates with the initial crack volume. a-f) Measured crack fraction (volume of cracks/voids divided by total volume, refer to Fig. 2b) using μCT plotted against rock depth. g-l) Quantified normalized crack fraction by initial crack volume (blue line a-f) plotted against rock depth.

3.2.2 Sustained freezing cycle (FT-2)

During the prolonged freezing experiment, the most significant crack growth was observed in the partially saturated rock sample, followed by the highly saturated one. In contrast, the low saturated sample exhibited minimal crack growth (Fig. 5d-f). The initial crack fraction at scan 0 ranged from $0.005^{+0.006}_{-0.003}$ for the low saturated sample, $0.01^{+0.008}_{-0.002}$ for the partially saturated sample, and $0.006^{+0.001}_{-0.001}$ for the highly saturated sample. The final crack fraction was $0.005^{+0.007}_{-0.003}$ (an increase of 0

15

%) for the low saturated sample, $0.012^{+0.008}_{-0.003}$ (an increase of 17 %) for the partially saturated rock, $0.006^{+0.001}_{-0.001}$ (an increase of 0 %)

Normalized data indicated the most pronounced crack growth in the partially saturated sample (Fig. 5j-l). The final scan revealed a mean normalized crack growth as 1.02 ±0.02 (indicating a 2% increase in crack volume) for the low saturated sample, 1.12 ±0.04 (12% increase) for the partially saturated sample, and 1.05 ±0.03 (5% increase) for the highly saturated sample.

4 Discussion

4.1 Critical discussion on AE Monitoring, stress modelling and µCT technique

Thermal and ice stresses or a combination of these stresses can cause rock damage. We monitored AE as a proxy for cracking as previous stress experiments (Eppes et al., 2016; Hallet et al., 1991) and analysed the timing of AE events in combination with simplified thermal stress and ice stress models to decipher the potential stress source. Our findings indicate a proportional relationship between the number of AE events and rock damage quantified via µCT (Fig. 6a,d) which was also shown by findings of Wang et al. (2020a). However, in our study the highest count of AE hits does not always align with the most visible rock damage (Fig. 6a). Specifically, the partially saturated sample exhibited over 415 AE hits with a normalized crack growth fraction of 47%, while the low saturated sample displayed 180 AE hits alongside a 53% crack growth. In contrast to our setup, Wang et al. (2020a) utilized a rock sample with artificially created macro fractures that predominantly drove the generation of AE signals. The discrepancy in our results might be due to variations in volume growth per crack propagation, potentially causing fewer AE releases with greater porosity growth. Additionally, the distinct responses of our natural rock samples to stress, influenced by slightly varying rock parameters, crack distribution and saturation, could also impact the number of AE hits. A potential alteration in the AE sensor's attachment to the rock might affect also signal detection. Although we reattached sensors and conducted lead break tests during the FT-1 cycle, the connection could have changed over time. Given the consistent AE accumulation trend observed in both the highly and low saturated samples, a likely coupling shift at the partially saturated sample is suggested (Fig. 3e), which was not reflected in µCT crack growth data (Fig. 5b, h). Despite these variables, the partially saturated sample showed before the shift already a higher AE accumulation than the less saturated one, underscoring that AE hits did not completely correlate with crack growth.

Our approach to model thermal stress did not account for the complex geometries of the cracks in the samples. As a result, our analysis concentrated on the timing of thermal stresses rather than their precise magnitudes. In our frost cracking modelling, we presented results for ellipsoidal cracks starting at a length of 1 mm. It is important to note, however, that cracks vary in size and exhibit more intricate geometries as seen by µCT imaging (Fig. 4). Additionally, slight variations in mechanical and elastic properties may occur since parameters were derived from different boulders of the same lithology or were based on data from Walder and Hallet (1985). Our sensitivity analysis (see Supplementary S1 and S2) for frost cracking models revealed

16

that the timing of increasing ice pressure was largely consistent across variations in parameters such as fracture toughness, growth law parameters, shear modulus, and Poisson's ratio. Nevertheless, the crack length significantly influences the timing

375 and the critical threshold for cracking. A larger crack length results in lower and delayed ice stresses, as well as a reduced critical threshold.

Prior µCT measurements have demonstrated the capability to quantify crack growth, as illustrated by Deprez et al. (2020b) in their study on highly porous (30-40%) oolithic limestone building stone, and by De Kock et al. (2015) in their examination of highly porous (~35%) miliolid limestone. These studies revealed the microscopic activities taking place within limestone pores

380 throughout freeze-thaw cycles. The authors linked the pore processes to potential patterns of macroscopic damage. In their experiments, both groups worked with small samples measuring 8-9 mm in diameter, achieving resolutions of 21 µm (Deprez et al., 2020b) and 20.4 µm (De Kock et al., 2015), respectively. In contrast, aiming to create a thermal gradient and water movement, we utilized larger samples, which led to a reduced spatial resolution of 60 µm. Our experiments demonstrated our capability to visualize and quantify damage in low-porosity rock samples caused by freeze-thaw cycles, while also

385 acknowledging the possibility of minor additional damage not detectable by µCT resolution. Previous laboratory freeze-thaw tests have used a decrease in elastic properties such as P-wave velocity, Young's modulus or increases in porosity (Whalley et al., 2004; Matsuoka, 1990; Draebing and Krautblatter, 2012) as a proxy for frost damage. Yet, detecting frost damage in low-porosity alpine rocks poses challenges due to the minimal or undetectable alterations in these elastic properties or porosity levels. Moreover, the use of measured elastic properties or porosities does not provide information on crack geometry and

390 crack growth. We demonstrated that cracks grow along pre-existing cracks and highlighted that µCT is a powerful analytical tool.

4.2 Influence of initial cracks on crack growth

In alpine rocks, freezing causes expansion in the pore spaces along existing cracks, influenced by the initial density of these

395 cracks. Although our samples were extracted from the same boulder and appeared to have a uniform distribution of cracks visually, µCT scanning revealed differences in the internal distribution of cracks across the samples. Our normalized µCT findings show a consistent increase in pore space expansion across the height of the samples, evident across pre-existing cracks through both freeze-thaw cycles. This uniform pattern indicates that the density of cracks plays a role in the extent of crack expansion, with a notable increase in crack growth linked to higher initial densities of cracks or pore volumes, as shown in

400 Fig. 5g-i. This finding is highlighted by the scan images (Fig. 4), which predominantly display the expansion of pore spaces within pre-existing cracks, as captured within the resolution of µCT. Our findings align with theoretical models proposed by Scherer (1999) and Walder and Hallet (1985), which suggest that ice crystallization pressure escalates in pore spaces, potentially leading to the enlargement of pores or cracks. This is further corroborated by microscopic analyses by Gerber et al. (2022), who confirmed that such pressure could indeed facilitate pore or crack expansion. Wang et al. (2020b), utilizing µCT

405 with a 35 µm resolution, found that pore space expansion in granite occurred exclusively as propagation of artificial created cracks, without evidence of new crack formation. Similarly, Dewanckele et al. (2013) observed no new crack formation within

the rock matrix through μCT imaging at a 2.5 μm resolution in high-porosity Lede and Noyant limestones, pinpointing that pore space growth transpires at pre-existing weak zones (such as fossils). We state that most frost damage occurs in preexisting cracks or voids and lead to crack propagation or widening with the process intensifying as crack density increases.
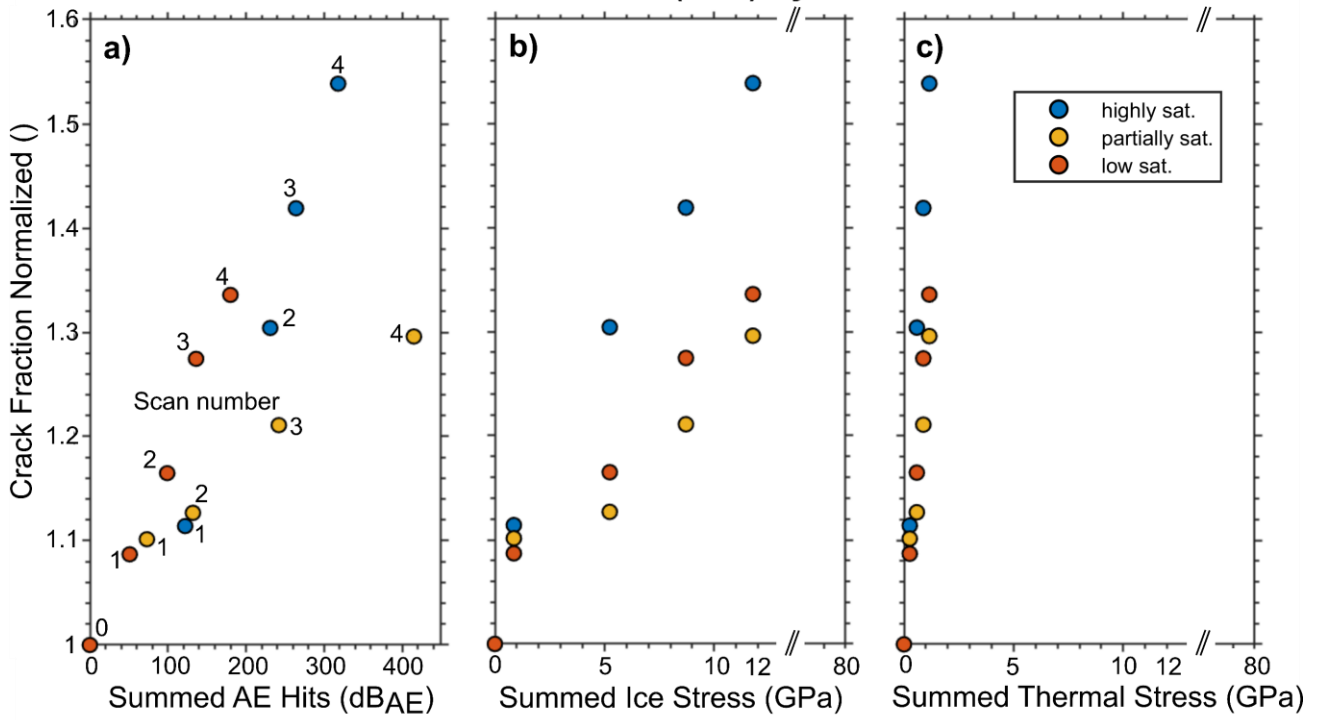
410

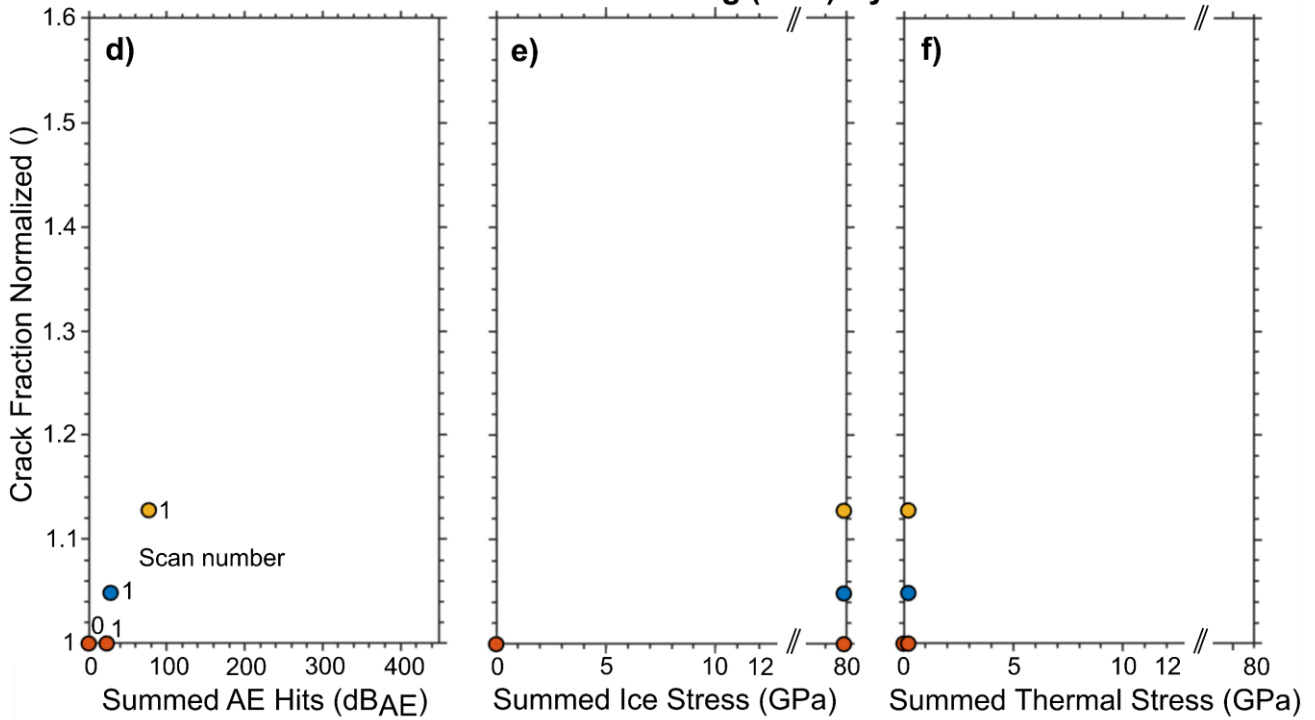### 4.3 Efficacy of freeze-thaw and sustained freezing cycles

Based on μCT data, freeze-thaw cycles (FT-1) revealed higher rock damage compared to a sustained freezing-cycle (FT-2) in low-porosity crack-dominated alpine rocks. Final crack growth is affected by initial crack density or pore volume distribution and cannot be compared directly; however, normalized crack growth fraction revealed an increase between 29 and 52 % for

415 FT-1 compared to an increase between 2 and 12 % for FT-2 (Fig. 6a, d). The increase varied between samples of different saturation levels. While the low number of samples prohibit a quantitative analysis of saturation effects on rock damage, our results are consistent and reveal higher damage of FT-1 compared to FT-2 independent of saturation levels (Fig. 6a, d).

Freeze-Thaw (FT-1) Cycles

a) Crack Fraction Normalized () vs Summed AE Hits (dBAE)

b) Summed Ice Stress (GPa)

c) Summed Thermal Stress (GPa)

highly sat.
partially sat.
low sat.

Scan number

Sustained Freezing (FT-2) Cycle

d) Crack Fraction Normalized () vs Summed AE Hits (dBAE)

Scan number

e) Summed Ice Stress (GPa)

f) Summed Thermal Stress (GPa)

420

The setup of FT-1 enables the development of thermal stresses during cooling and warming of the samples, volumetric

425 expansion alongside the expanding freezing front and ice segregation during freezing conditions (Fig. 7a). In addition, FT-2 favours the development of ice segregation when temperatures are sustained, and rock moisture is able to migrate towards the freezing front (Fig. 7a).

During warming and cooling thermal stresses with a magnitude slightly higher than 1 MPa occurred. Due to the higher number

430 of temperature cycles in FT-1, higher cumulative thermal stresses occurred in FT-1 than FT-2 (Fig. 6c,f), which could contribute to the increased rock damage observed and quantified via µCT (Fig. 5g-l). Nonetheless, when compared to the predicted ice stresses (Fig. 6b,e) or accumulated AE hits during freezing times (Fig. 7), the thermal stresses were significantly lower, pointing to frost cracking as the predominant cause of rock damage.

Simulated stresses by our frost cracking models are higher for FT-2 in comparison to FT-1 (Fig. 6b,e) which is not supported

435 by our µCT findings (Fig. 5g-l). Our frost cracking modelling revealed eight times higher ice stresses in the sustained freezing phase than the freeze-thaw cycle. A fundamental requirement for our frost cracking model is complete saturation, a condition not consistently met throughout the experiment due to evaporation affecting our samples. The highly saturated samples showed in contrast to our model predictions, that highest frost damage (+53 % more crack volume than initially) occurred during FT-1, whilst in FT-2 significantly less crack growth (+5 % more crack volume than initially) was observed (Fig. 5i,l). This

440 observation could potentially be explained by variations in ice formation. Gerber et al. (2023) suggests that the pressures exerted by ice depend on its structure, which in turn is influenced by the rate of ice formation and its aging process. Rapid freeze-thaw cycles may result in fine-grained ice and a sharp increase in stresses, whereas prolonged freezing, through aging, may result in coarse ice grains exerting less stress. Nevertheless, the transformation and aging of ice over an extended period of freezing – a characteristic of alpine conditions – could result in an increase in ice stress, thereby enhancing the potential for

445 frost damage. A different explanation could be that ice segregation relies on water migration towards the freezing front, facilitated by the presence of unfrozen water at the top of our samples. Gerber et al. (2023) indicate that various ice structures could affect water migration needed for ice segregation differently lowering its impact. Prick (1997) noted water migration in limestone samples similar in size, with porosities ranging from 26 to 48.2 %. In contrast, our rock samples exhibit much lower porosities of around 0.1%, offering a substantially smaller water reservoir. This suggests that the water supply in FT-2 may

450 have been also a limiting factor for ice segregation, despite the temperature conditions being conducive to this process (e.g. Walder and Hallet, 1985). As a result, our simulations of ice stress might have overestimated the actual stresses involved. In addition, our frost cracking model simplified the complex crack geometries observed in the samples (Fig. 4). Therefore, the

magnitude of simulated ice stresses potentially deviates significantly from occurred ice stresses which resulted in the deviation between modelled ice stresses and measured rock damage especially in FT-2 (Fig. 6b,e).

455   During freezing of water to ice, volume expansion occurs that can produce rock damage if saturation levels are above 91%. The high number of freezing cycles in FT-1 could result in more volume expansion induced frost cracking as in FT-2. The full saturated sample in FT-1 revealed the highest normalized rock damage (53 %) compared to partially (29% increase) and low (34% increase) saturated samples (Fig. 5g,h), which could indicate the involvement of volumetric expansion. We only estimated initial saturation and rock moisture can redistribute during the experiments resulting in higher moisture levels at the

460   freezing fronts that could exceed moisture threshold enabling volume expansion induced damage. In addition to volume expansion, higher saturation can also increase the efficacy of ice segregation by providing more moisture able to migrate. We conclude that within the constraints of our experiments freeze-thaw cycles cause higher frost damage compared to sustained freezing cycles with ice segregation serving as the primary contributing factor to frost cracking while the occurrence of volume expansion induced damage is likely within high saturated samples and cannot be exclude in low and partially saturated samples.

465
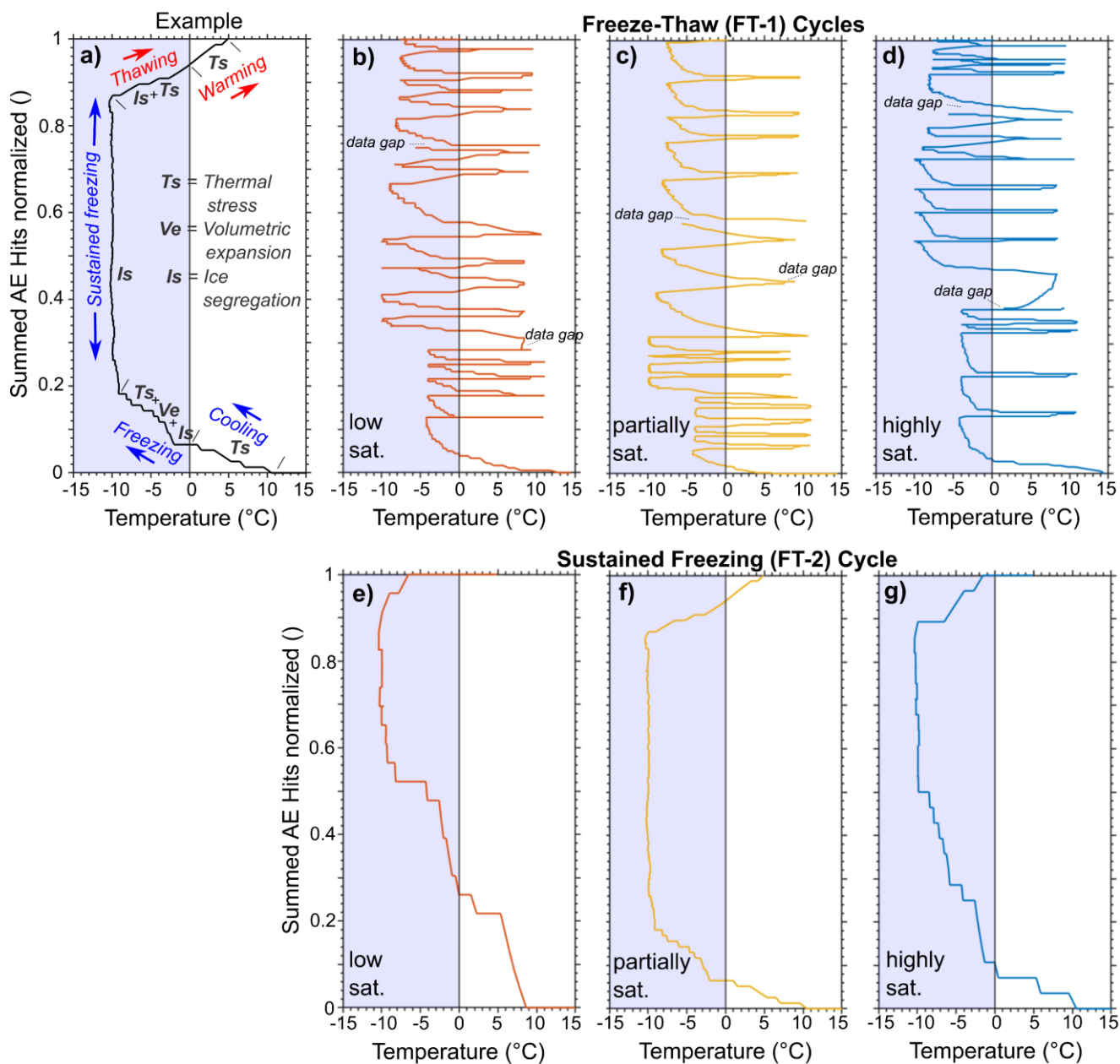
Figure. 7: Cooling phases accumulate more AE hits compared to warming phases, suggesting frost cracking as the main contributor to rock damage. a) Timing examples of potential stress occurrences include thermal stresses during sample cooling and warming, volumetric expansion along with the expanding freezing front, and ice segregation under freezing conditions. Cumulative AE hits are plotted against the bottom rock temperature sensor for b-d) FT-1 and e-g) FT-2.

475

22

4.4 Implications for alpine rockwalls

Our results revealed that the presence and arrangement of voids and fractures within rock significantly impact frost damage. We have shown that micro-crack expansion tends to follow pre-existing fractures, extending their width and length (Fig. 4 and 5g-l), leading to a gradual increase in crack size. As a result, samples with a higher crack density experience more severe frost damage. In natural rockwalls, both micro and macro cracks are present, the latter often arising from tectonic forces and/or weathering effects. These fractures play a crucial role for erosion processes as they influence rock cohesion and modify the dynamics, patterns, and locations of geomorphic activities on various spatial and temporal scales (Scott and Wohl, 2019). Studies by Hales and Roering (2009) and Draebing and Mayer (2021) have established a link between frost cracking intensity and the density of fractures, with rockwalls exhibiting more fractures also showing greater evidence of frost cracking. Furthermore, Eppes et al. (2018) have demonstrated through both field and laboratory observations that an increase in the length and quantity of cracks leads to higher long-term erosion rates. Neely et al. (2019) revealed that higher fracture density decreases steepness of cliffs and increases catchment erosion rates. In New Zealand, Clarke and Burbank (2010) showed that bedrock fracturing by geomorphic processes including weathering controls the depths of erosive processes as bedrock landsliding. We infer that upscaling our findings from micro to macro cracks highlights the connection between erosion and fracture density. However, such extrapolation must consider the scale dependencies and complex fracture interactions influenced by broader geological and environmental factors, including tectonic forces, weathering effects, and variations in material properties, which could significantly modify erosion dynamics beyond micro-scale observations.

Our findings indicate that frost cracking is more effective during freeze-thaw cycles than during prolonged periods of freezing. Matsuoka et al. (1998) indicated that south-facing rockwalls typically undergo more freeze-thaw cycles due to lack of snow cover, whereas those facing north are subject to longer durations of freezing. This leads to the initial assumption that south facing rockwalls would sustain more frost damage, contributing to increased erosion. However, few existing empirical data indicates that erosion rates are actually 2.5 to 3 times (Sass, 2005b) or up to one magnitude (Coutard and Francou, 1989) higher on north-facing rockwalls. Matsuoka et al. (1998) suggested that while freeze-thaw cycles can cause shallow frost damage (up to 0.3 m deep), prolonged freezing can result in more significant frost damage (up to 5 m deep), leading to larger rockfalls. This indicates that the temporal scale of freeze-thaw cycles plays a crucial role in determining weathering and erosion rates, a concept further supported by Matsuoka (2008), who found that short-term freeze-thaw cycles cause minor crack expansion, whereas long-term freezing leads to more substantial crack widening.

Our research suggests a direct correlation between the frequency of AE events and the extent of rock damage, as measured by μCT scanning. However, the highest occurrences of AE hits do not consistently correspond to the most significant observable rock damage. This discrepancy could be attributed to ice formation influenced by thermal gradients, as well as changes and aging in the ice, as discussed by Gerber et al. (2023). This insight has implications for studies that employ AE as an indicator for thermal stress-induced cracking (Eppes et al., 2016; Collins et al., 2018) and frost cracking (Amitrano et al., 2012; Girard et al., 2013) in natural rockwalls.

The estimated ice stresses in our simulations may significantly diverge from the actual ice stresses experienced, leading to differences between simulated ice stresses and observed rock damage, particularly in the FT-2 scenario. This mismatch between model predictions and actual frost damage observations could stem from the model's oversimplified representations of crack geometries and rock properties, or the relatively brief duration of sustained freezing in FT-2 when compared to conditions on a real rockwall. Research efforts such as those by Draebing and Mayer (2021) or Sanders et al. (2012) which utilize frost cracking models to assess frost damage, might have overemphasized the effects of frost weathering. Nonetheless, Draebing et al. (2022) showed that frost weathering simulations do correspond with the erosion rates observed on north-facing rockwalls, where extended periods of freezing are more common.

5 Conclusion

In our investigation of frost-induced damage on Dachstein limestone, we employed X-ray computed micro-tomography (μCT), acoustic emission (AE) monitoring, and frost cracking modelling to assess the damage. We aimed to distinguish between different mechanisms of rock damage by simulating thermal and ice-induced stresses and correlating them with AE activity in samples with varying saturation levels. Our research demonstrated that μCT effectively measures frost damage in low-porosity (0.1%) rock, primarily revealing damage through the expansion or deepening of existing cracks rather than the creation of new ones. Our findings also revealed that the presence and distribution of voids and cracks significantly influence frost damage, with rocks having a higher initial crack density exhibiting more damage. A direct link was found between the rate of AE events and the degree of rock damage as determined by μCT, however, the most frequent AE hits did not always match the areas of greatest visible damage, suggesting complexities in the relationship between AE activity and rock damage.

Our studies suggest that rock damage is primarily a result of thermal stresses and frost cracking during cooling phases, with frost cracking identified as a key contributor to damage. Yet, the ice stresses predicted by our simulations might greatly differ from the actual stresses, potentially due to the model's simplified assumptions or the short duration of sustained freezing in our FT-2 scenario. Analysis of μCT data revealed that repeated freeze-thaw cycles (FT-1) resulted in more effective cracking compared to extended periods of freezing (FT-2). This observation contrasts with field study outcomes that associate frost damage and rockwall erosion, showing greater erosion rates on north-facing rockwalls, which typically undergo longer periods of sustained freezing rather than freeze-thaw cycles. We assume that the limited water accessibility in FT-2, due to the samples' low porosity or the dynamics of ice formation, and the short experiment time might explain this discrepancy. Given the finite sample size and varied saturation levels, our experiments suggest that higher levels of saturation tend to increase frost-induced rock damage, as inferred from acoustic emission activity. This preliminary evidence emphasizes the need for additional research to fully understand saturation's impact on frost damage.

Data availability

Data is available at UU depository: https://public.yoda.uu.nl/geo/UU01/OLMSN0.html

Code for frost cracking modelling is available at: https://github.com/TillM90/Code_frost_cracking_model.git

Author Contribution

TM, MD, LS and DD designed the experiments. TM, MD and LS conducted the experiments and TM processed the data with support by MD and LS. TM and DD wrote the manuscript with contributions from MD, LS and VC.

Conflict of Interest Statement

The authors declare that they have no conflict of interest.

Acknowledgements

References

1097-6:2022-5, D.-E.: Tests for mechanical and physical properties of aggregates - Part 6: Determination of particle density and water absorption; German version EN 1097-6:2022, 64 pp., https://dx.doi.org/10.31030/3290441,

52102:2006-02, D.-E.: Test methods for aggregates - Determination of dry bulk density by the cylinder method and calcualtion of the ratio of density, 9 pp.

Amitrano, D., Gruber, S., and Girard, L.: Evidence of frost-cracking inferred from acoustic emissions in a high-alpine rock-wall, Earth and Planetary Science Letters, 341-344, 86-93, https://dx.doi.org/10.1016/j.epsl.2012.06.014, 2012.

Anderson, R. S.: Near-surface thermal profiles in alpine bedrock: Implications for the frost weathering of rock, Arct. Alp. Res., 30, 362-372, https://dx.doi.org/10.2307/1552008, 1998.

Bazant, Z. P. and Planas, J.: Fracture and Size Effect in Concrete and Other Quasibrittle Materials 1st, New York, https://dx.doi.org/10.1201/9780203756799 1998.

Carloni, C., Santandrea, M., and Baietti, G.: Influence of the width of the specimen on the fracture response of concrete notched beams, Engineering Fracture Mechanics, 216, 106465, https://dx.doi.org/10.1016/j.engfracmech.2019.04.039, 2019.

Cermák, V. and Rybach, L.: Thermal conductivity and specific heat of minerals and rocks, in: Landolt–Börnstein Zahlenwerte and Funktionen aus Naturwissenschaften und Technik, Neue Serie, Physikalische Eigenschaften der Gesteine (V/1a), edited by: Angeneister, G., Springer, Berlin, 305–343, 1982.

Clarke, B. A. and Burbank, D. W.: Bedrock fracturing, threshold hillslopes, and limits to the magnitude of bedrock landslides, Earth and Planetary Science Letters, 297, 577-586, https://doi.org/10.1016/j.epsl.2010.07.011, 2010.

580 Cnudde, V. and Boone, M.: High-resolution X-ray computed tomography in geosciences: a review of the current technology and applications, EARTH-SCIENCE REVIEWS, 123, 1-17, 10.1016/j.earscirev.2013.04.003, 2013.

Collins, B. D., Stock, G. M., Eppes, M.-C., Lewis, S. W., Corbett, S. C., and Smith, J. B.: Thermal influences on spontaneous rock dome exfoliation, Nature Communications, 9, 762, https://dx.doi.org/10.1038/s41467-017-02728-1, 2018.

Coutard, J.-P. and Francou, B.: Rock Temperature Measurements in Two Alpine Environments: Implications for Frost Shattering, Arct. Alp.
585 Res., 21, 399-416, https://dx.doi.org/10.2307/1551649, 1989.

De Kock, T., Boone, M. A., De Schryver, T., Van Stappen, J., Derluyn, H., Masschaele, B., De Schutter, G., and Cnudde, V.: A Pore-Scale Study of Fracture Dynamics in Rock Using X-ray Micro-CT Under Ambient Freeze–Thaw Cycling, Environmental Science & Technology, 49, 2867-2874, https://dx.doi.org/10.1021/es505738d, 2015.

Deprez, M., De Kock, T., De Schutter, G., and Cnudde, V.: The role of ink-bottle pores in freeze-thaw damage of oolithic limestone,
590 Construction and Building Materials, 246, 118515, https://dx.doi.org/10.1016/j.conbuildmat.2020.118515, 2020a.

Deprez, M., De Kock, T., De Schutter, G., and Cnudde, V.: A review on freeze-thaw action and weathering of rocks, Earth-Science Reviews, 203, 103143, https://dx.doi.org/10.1016/j.earscirev.2020.103143, 2020b.

Derjaguin, B. V. and Churaev, N. V.: Flow of nonfreezing water interlayers and frost heaving, Cold Regions Science and Technology, 12, 57-66, https://dx.doi.org/10.1016/0165-232X(86)90020-0, 1986.

595 Dewanckele, J., Boone, M. A., De Kock, T., De Boever, W., Brabant, L., Boone, M. N., Fronteau, G., Dils, J., Van Hoorebeke, L., Jacobs, P., and Cnudde, V.: Holistic approach of pre-existing flaws on the decay of two limestones, Science of The Total Environment, 447, 403-414, https://doi.org/10.1016/j.scitotenv.2012.12.094, 2013.

Draebing, D.: Identification of rock and fracture kinematics in high Alpine rockwalls under the influence of elevation, Earth Surface Dynamics, 9, 977-994, https://dx.doi.org/10.5194/esurf-9-977-2021, 2021.

600 Draebing, D. and Krautblatter, M.: P-wave velocity changes in freezing hard low-porosity rocks: a laboratory-based time-average model, The Cryosphere, 6, 1163-1174, https://dx.doi.org/10.5194/tc-6-1163-2012, 2012.

Draebing, D. and Krautblatter, M.: The Efficacy of Frost Weathering Processes in Alpine Rockwalls, Geophysical Research Letters, 46, 6516-6524, https://dx.doi.org/10.1029/2019gl081981, 2019.

Draebing, D. and Mayer, T.: Topographic and geologic controls on frost cracking in Alpine rockwalls, Journal of Geophysical Research:
605 Earth Surface, 126, e2021JF006163, https://dx.doi.org/10.1029/2021JF006163, 2021.

Draebing, D., Krautblatter, M., and Hoffmann, T.: Thermo-cryogenic controls of fracture kinematics in permafrost rockwalls, Geophysical Research Letters, 44, 3535-3544, https://dx.doi.org/10.1002/2016GL072050, 2017a.

Draebing, D., Mayer, T., Jacobs, B., and McColl, S. T.: Alpine rockwall erosion patterns follow elevation-dependent climate trajectories, Communications Earth & Environment, 3, 21, https://dx.doi.org/10.1038/s43247-022-00348-2, 2022.

610 Draebing, D., Haberkorn, A., Krautblatter, M., Kenner, R., and Phillips, M.: Thermal and Mechanical Responses Resulting From Spatial and Temporal Snow Cover Variability in Permafrost Rock Slopes, Steintaelli, Swiss Alps, Permafrost and Periglacial Processes, 28, 140-157, https://dx.doi.org/10.1002/ppp.1921, 2017b.

Duca, S., Occhiena, C., Mattone, M., Sambuelli, L., and Scavia, C.: Feasibility of Ice Segregation Location by Acoustic Emission Detection: A Laboratory Test in Gneiss, Permafrost And Periglacial Processes, 25, 208-219, 10.1002/ppp.1814, 2014.

615 Egholm, D. L., Andersen, J. L., Knudsen, M. F., Jansen, J. D., and Nielsen, S. B.: The periglacial engine of mountain erosion - Part 2: Modelling large-scale landscape evolution, Earth Surface Dynamics, 3, 463-482, https://dx.doi.org/10.5194/esurf-3-463-2015, 2015.

Eppes, M.-C. and Keanini, R.: Mechanical weathering and rock erosion by climate-dependent subcritical cracking, Reviews of Geophysics, 55, 470-508, https://dx.doi.org/10.1002/2017RG000557, 2017.

Eppes, M. C., Magi, B., Hallet, B., Delmelle, E., Mackenzie-Helnwein, P., Warren, K., and Swami, S.: Deciphering the role of solar-induced
620 thermal stresses in rock weathering, Geological Society of America Bulletin, 128, 1315-1338, https://dx.doi.org/10.1130/b31422.1, 2016.

Eppes, M. C., Hancock, G. S., Chen, X., Arey, J., Dewers, T., Huettenmoser, J., Kiessling, S., Moser, F., Tannu, N., Weiserbs, B., and Whitten, J.: Rates of subcritical cracking and long-term rock erosion, Geology, 46, 951-954, 10.1130/G45256.1, 2018.

Eslami, J., Walbert, C., Beaucour, A.-L., Bourges, A., and Noumowe, A.: Influence of physical and mechanical properties on the durability of limestone subjected to freeze-thaw cycles, Construction and Building Materials, 162, 420-429,
625 https://dx.doi.org/10.1016/j.conbuildmat.2017.12.031, 2018.

Everett, D. H.: The thermodynamics of frost damage to porous solids, Transactions of the Faraday Society, 57, 1541-1551, https://dx.doi.org/10.1039/TF9615701541, 1961.

Gerber, D., Wilen, L. A., Dufresne, E. R., and Style, R. W.: Polycrystallinity Enhances Stress Buildup around Ice, Physical Review Letters, 131, 208201, 10.1103/PhysRevLett.131.208201, 2023.

630 Gerber, D., Wilen, L. A., Poydenot, F., Dufresne, E. R., and Style, R. W.: Stress accumulation by confined ice in a temperature gradient, Proc Natl Acad Sci U S A, 119, e2200748119, https://dx.doi.org/10.1073/pnas.2200748119, 2022.

Gilpin, R. R.: A model of the "liquid-like" layer between ice and a substrate with applications to wire regelation and particle migration, Journal of Colloid and Interface Science, 68, 235-251, https://dx.doi.org/10.1016/0021-9797(79)90277-7, 1979.

Gilpin, R. R.: A model for the prediction of ice lensing and frost heave in soils, Water Resources Research, 16, 918-930,
635 https://dx.doi.org/10.1029/WR016i005p00918, 1980.

Girard, L., Gruber, S., Weber, S., and Beutel, J.: Environmental controls of frost cracking revealed through in situ acoustic emission measurements in steep bedrock, Geophysical Research Letters, 40, 1748-1753, https://dx.doi.org/10.1002/grl.50384, 2013.

Hales, T. C. and Roering, J. J.: A frost "buzzsaw" mechanism for erosion of the eastern Southern Alps, New Zealand, Geomorphology, 107, 241-253, https://dx.doi.org/10.1016/j.geomorph.2008.12.012, 2009.

640 Hallet, B., Walder, J. S., and Stubbs, C. W.: Weathering by segregation ice growth in microcracks at sustained subzero temperatures: Verification from an experimental study using acoustic emissions, Permafrost And Periglacial Processes, 2, 283-300, https://dx.doi.org/10.1002/ppp.3430020404, 1991.

Jia, H., Xiang, W., and Krautblatter, M.: Quantifying Rock Fatigue and Decreasing Compressive and Tensile Strength after Repeated Freeze-Thaw Cycles, Permafrost and Periglacial Processes, 26, 368-377, https://dx.doi.org/10.1002/ppp.1857, 2015.

645 Kjelstrup, S., Ghoreishian Amiri, S. A., Loranger, B., Gao, H., and Grimstad, G.: Transport coefficients and pressure conditions for growth of ice lens in frozen soil, Acta Geotechnica, 16, https://dx.doi.org/10.1007/s11440-021-01158-0, 2021.

Lepique, M.: Empfehlung Nr. 10 des Arbeitskreises 3.3 "Versuchstechnik Fels" der Deutschen Gesellschaft für Geotechnik e. V.: Indirekter Zugversuch an Gesteinsproben – Spaltzugversuch, Bautechnik, 85, 623-627, https://dx.doi.org/10.1002/bate.200810048, 2008.

Maji, V. and Murton, J. B.: Micro-computed tomography imaging and probabilistic modelling of rock fracture by freeze–thaw, Earth Surface

650 Processes and Landforms, 45, 666-680, https://doi.org/10.1002/esp.4764, 2020.

Maji, V. and Murton, J. B.: Experimental Observations and Statistical Modeling of Crack Propagation Dynamics in Limestone by Acoustic Emission Analysis During Freezing and Thawing, Journal of Geophysical Research: Earth Surface, 126, e2021JF006127, https://dx.doi.org/10.1029/2021JF006127, 2021.

Matsuoka, N.: Mechanisms of rock breakdown by frost action: An experimental approach, Cold Regions Science and Technology, 17, 253-

655 270, https://dx.doi.org/10.1016/S0165-232X(05)80005-9, 1990.

Matsuoka, N.: Microgelivation versus macrogelivation: towards bridging the gap between laboratory and field frost weathering, Permafrost and Periglacial Processes, 12, 299-313, https://dx.doi.org/10.1002/ppp.393, 2001.

Matsuoka, N.: Frost weathering and rockwall erosion in the southeastern Swiss Alps: Long-term (1994-2006) observations, Geomorphology, 99, 353-368, 10.1016/j.geomorph.2007.11.013, 2008.

660 Matsuoka, N.: A multi-method monitoring of timing, magnitude and origin of rockfall activity in the Japanese Alps, Geomorphology, 336, 65-76, https://dx.doi.org/10.1016/j.geomorph.2019.03.023, 2019.

Matsuoka, N. and Murton, J.: Frost weathering: Recent advances and future directions, Permafrost And Periglacial Processes, 19, 195-210, https://dx.doi.org/10.1002/ppp.620, 2008.

Matsuoka, N., Hirakawa, K., Watanabe, T., Haeberli, W., and Keller, F.: THE ROLE OF DIURNAL, ANNUAL AND MILLENNIAL

665 FREEZE-THAW CYCLES IN CONTROLLING ALPINE SLOPE INSTABILITY,

Mayer, T., Eppes, M., and Draebing, D.: Influences Driving and Limiting the Efficacy of Ice Segregation in Alpine Rocks, Geophysical Research Letters, 50, e2023GL102951, https://dx.doi.org/10.1029/2023GL102951, 2023.

Messenzehl, K., Viles, H., Otto, J.-C., Ewald, A., and Dikau, R.: Linking rock weathering, rockwall instability and rockfall supply on talus slopes in glaciated hanging valleys (Swiss Alps), Permafrost and Periglacial Processes, 29, 135-151, 10.1002/ppp.1976, 2018.

670 Murton, J. B., Peterson, R., and Ozouf, J.-C.: Bedrock Fracture by Ice Segregation in Cold Regions, Science, 314, 1127-1129, https://dx.doi.org/10.1126/science.1132127, 2006.

Neely, A. B., DiBiase, R. A., Corbett, L. B., Bierman, P. R., and Caffee, M. W.: Bedrock fracture density controls on hillslope erodibility in steep, rocky landscapes with patchy soil cover, southern California, USA, Earth and Planetary Science Letters, 522, 186-197, https://doi.org/10.1016/j.epsl.2019.06.011, 2019.

675 Paul, G. C. D.: Materials science & engineering, CRC Press, Materials Park, Ohio:ASM International1991.

Perras, M. A. and Diederichs, M. S.: A Review of the Tensile Strength of Rock: Concepts and Testing, Geotechnical and Geological Engineering, 32, 525-546, https://dx.doi.org/10.1007/s10706-014-9732-0, 2014.

Pfiffner, O. A.: Geologie der Alpen, Haupt 359 pp., 10.36198/9783838584164, 2010.

Prick, A.: Critical Degree of Saturation as a Threshold Moisture Level in Frost Weathering of Limestones, Permafrost and Periglacial

680 Processes, 8, 91-99, https://dx.doi.org/10.1002/(SICI)1099-1530(199701)8:1<91::AID-PPP238>3.0.CO;2-4, 1997.

Sanders, J. W., Cuffey, K. M., Moore, J. R., MacGregor, K. R., and Kavanaugh, J. L.: Periglacial weathering and headwall erosion in cirque glacier bergschrunds, Geology, 40, 779-782, https://dx.doi.org/10.1130/g33330.1, 2012.

Sass, O.: Rock moisture measurements: techniques, results, and implications for weathering, Earth Surface Processes and Landforms, 30, 359-374, https://dx.doi.org/10.1002/esp.1214, 2005a.

685 Sass, O.: Spatial patterns of rockfall intensity in the northern Alps, Zeitschrift für Geomorphologie, Supplementary Issues, 138, 51-65, 2005b.

Scherer, G. W.: Crystallization in pores, Cement and Concrete Research, 29, 1347-1358, https://dx.doi.org/10.1016/S0008-8846(99)00002-2, 1999.

Scott, D. N. and Wohl, E. E.: Bedrock fracture influences on geomorphic process and form across process domains and scales, Earth Surface

690 Processes and Landforms, 44, 27-45, https://doi.org/10.1002/esp.4473, 2019.

Sibley, D. N., Llombart, P., Noya, E. G., Archer, A. J., and MacDowell, L. G.: How ice grows from premelting films and water droplets, Nature Communications, 12, 239, https://dx.doi.org/10.1038/s41467-020-20318-6, 2021.

Walder, J. and Hallet, B.: A Theoretical-Model of the Fracture of Rock During Freezing, Geological Society of America Bulletin, 96, 336-346, https://dx.doi.org/10.1130/0016-7606(1985)96<336:ATMOTF>2.0.CO;2, 1985.

695   Walder, J. S. and Hallet, B.: The Physical Basis of Frost Weathering - toward a More Fundamental and Unified Perspective, Arct. Alp. Res., 18, 27-32, https://dx.doi.org/10.2307/1551211, 1986.

Wang, Y., Han, J. Q., and Li, C. H.: Acoustic emission and CT investigation on fracture evolution of granite containing two flaws subjected to freeze–thaw and cyclic uniaxial increasing-amplitude loading conditions, Construction and Building Materials, 260, 119769, https://doi.org/10.1016/j.conbuildmat.2020.119769, 2020a.

700   Wang, Y., Feng, W. K., Wang, H. J., Li, C. H., and Hou, Z. Q.: Rock bridge fracturing characteristics in granite induced by freeze-thaw and uniaxial deformation revealed by AE monitoring and post-test CT scanning, Cold Regions Science and Technology, 177, 103115, https://doi.org/10.1016/j.coldregions.2020.103115, 2020b.

Webber, J. B. W., Dore, J. C., Strange, J. H., Anderson, R., and Tohidi, B.: Plastic ice in confined geometry: the evidence from neutron diffraction and NMR relaxation, Journal of Physics: Condensed Matter, 19, 415117, https://dx.doi.org/10.1088/0953-8984/19/41/415117,

705   2007.

Whalley, W. B., Rea, B. R., and Rainey, M. M.: Weathering, Blockfields, and Fracture Systems and the Implications for Long-Term Landscape Formation: Some Evidence from Lyngen and Øksfordjøkelen Areas in North Norway, Polar Geography, 28, 93-119, https://dx.doi.org/10.1080/789610120, 2004.

Withers, P. J., Bouman, C., Carmignato, S., Cnudde, V., Grimaldi, D., Hagen, C. K., Maire, E., Manley, M., Du Plessis, A., and Stock, S.

710   R.: X-ray computed tomography, Nature Reviews Methods Primers, 1, 18, 10.1038/s43586-021-00015-4, 2021.